Rapid Communications | Editors' Suggestion

Band engineering of a magnetic thin film rare-earth monopnictide: A platform for high Chern number

Hisashi Inoue,[1,*] Minyong Han,[1] Mengli Hu,[2] Takehito Suzuki,[1] Junwei Liu,[2,†] and Joseph G. Checkelsky[1,‡]
[1]*Department of Physics, Massachusetts Institute of Technology, Cambridge, Massachusetts 02139, USA*
[2]*Department of Physics, Hong Kong University of Science and Technology, Clear Water Bay, Hong Kong, China*

(Received 2 May 2019; revised manuscript received 21 July 2019; published 21 October 2019)

Realizing quantum materials in few atomic layer morphologies is a key to both observing and controlling a wide variety of exotic quantum phenomena. This includes topological electronic materials, where the tunability and dimensionality of few layer materials have enabled the detection of Z_2, Chern, and Majorana phases. Here we report the development of a platform for thin film correlated, topological states in the magnetic rare-earth monopnictide (RX) system GdBi synthesized by molecular beam epitaxy. This material is known from bulk single crystal studies to be semimetallic antiferromagnets with Neel temperature $T_N = 28$ K and is the magnetic analog of the non-f-electron containing system LaBi proposed to have topological surface states. Our transport and magnetization studies of thin films grown epitaxially on BaF_2 reveal that semimetallicity is lifted below approximately eight crystallographic unit cells while magnetic order is maintained down to our minimum thickness of five crystallographic unit cells. First-principles calculations show that the nontrivial topology is preserved down to the monolayer limit, where quantum confinement and the lattice symmetry give rise to a $C = 2$ Chern insulator phase. We further demonstrate the stabilization of these films against atmospheric degradation using a combination of air-free buffer and capping procedures. These results together identify thin-film RX materials as potential platforms for engineering topological electronic bands in correlated magnetic materials.

DOI: 10.1103/PhysRevMaterials.3.101202

I. INTRODUCTION

The rare-earth monopnictides (RX, where R and X denote the rare-earth and pnictogen elements) are a class of materials which host a rich variety of magnetic and electronic phases ranging from ferromagnetic semiconductors to antiferromagnetic semimetals [1,2]. Recent studies have shown that for X = Bi the large spin-orbit coupling results in band inversion and topologically protected surface states [3–12]. Given the strong coupling between the conduction electrons and localized magnetic moments of RX systems, this offers the opportunity to study the nontrivial electronic topology of correlated electrons [13–17]. A challenge for these systems is the significant semimetallic band overlap of the conduction and valence bands (described below), which for transport studies precludes the isolation of the surface response. However, while realization of few monolayer morphologies has proven to be a powerful method to remove parasitic bulk conductance from unintentional doping in conventional three-dimensional topological insulators (TIs) [18–21], theoretical calculations of RX systems in this limit suggest further that quantum confinement has the potential to energetically isolate the topologically nontrivial bands [22].

Here we report the synthesis and study of epitaxial thin films of the R = Gd compound GdBi and show that it can be engineered toward an insulator by two-dimensional (2D) quantum confinement while retaining its magnetic and topological properties. As shown in Fig. 1(a), GdBi has a rock-salt structure (space group $Fm\bar{3}m$) and hosts type-II antiferromagnetic (AFM) order below $T_N = 28$ K [1,23] with Gd moments ferromagnetically aligned within the {111} planes and antiferrromagnetically stacked along the ⟨111⟩ directions [24]. The electronic band structure in the vicinity of the Fermi level E_F consists of a Gd 5d-derived conduction band around the X points and two Bi 6p-derived valence bands around the Γ point [see Fig. 1(b)]. These bands overlap by approximately 1 eV, thus constituting a semimetal. Midway in momentum between Γ and X a band crossing occurs, which when hybridized by spin-orbit coupling is proposed to give rise to a topologically nontrivial gap [3]. This spin-orbit induced gap also offers a possibility for realizing Weyl nodes in the magnetic phase of GdBi in an applied field, taking advantage of strong exchange splitting in a canted configuration [Fig. 1(b) inset] [25–28].

While photoemission studies of bulk single crystals have proven instrumental for determining the bulk and surface electronic structure of the RX systems [2,4–6,8,9,29], as noted above it is of significant interest to realize few monolayer morphologies of these materials to study their transport properties as well as enable *in situ* control via electrostatic gates. Given their cubic rock-salt structure, this is most appropriately achieved by thin film growth, which we employ here via molecular beam epitaxy (MBE). Subsequent structural, electrical transport, and magnetic characterization demonstrate

*Present address: Frontier Research Institute for Interdisciplinary Sciences and Institute for Materials Research, Tohoku University, Sendai 980-8577, Japan.
†liuj@ust.hk
‡checkelsky@mit.edu

the high quality of these materials. First-principles band structure calculations confirm that nontrivial topology remains upon confinement and leads to a $C = 2$ Chern insulator phase in the monolayer limit. These suggest that thin-film GdBi may be an ideal platform to investigate correlation between magnetism and topologically nontrivial surface states [13].

II. FABRICATION OF GDBI EPITAXIAL THIN FILMS BY MBE

High quality epitaxial thin films of GdBi (111) were synthesized by MBE. The overall structure is summarized in Fig. 1(c) with an optical photograph of a typical film shown in Fig. 1(d). Single crystalline BaF_2 (111) is used for the substrate, which has a cubic lattice constant $a_{BaF2} = 0.620$ nm well matched with that of GdBi $a_{GdBi} = 0.632$ nm. Prior to GdBi deposition, 200 nm of an epitaxial BaF_2 (111) buffer layer was deposited to improve surface flatness. As shown in Figs. 1(e) and 1(f), atomic force microscope (AFM) images of the BaF_2 buffer layer show a smooth surface with atomically flat terraces and steps with height corresponding to the spacing between successive (111) planes of BaF_2. The GdBi (111) layer was grown at temperature $T = 400^\circ$ C with the thickness varied from $t_{GdBi} = 5$ to 40 nm. Finally, the structure was capped with 40 to 100 nm of epitaxial BaF_2 [30]. Samples were transferred into a glovebox directly after the growth without air exposure and capped either by AlN layer deposited by atomic layer deposition or by a nonaqueous liquid. This prevents sample degradation during subsequent measurements [30].

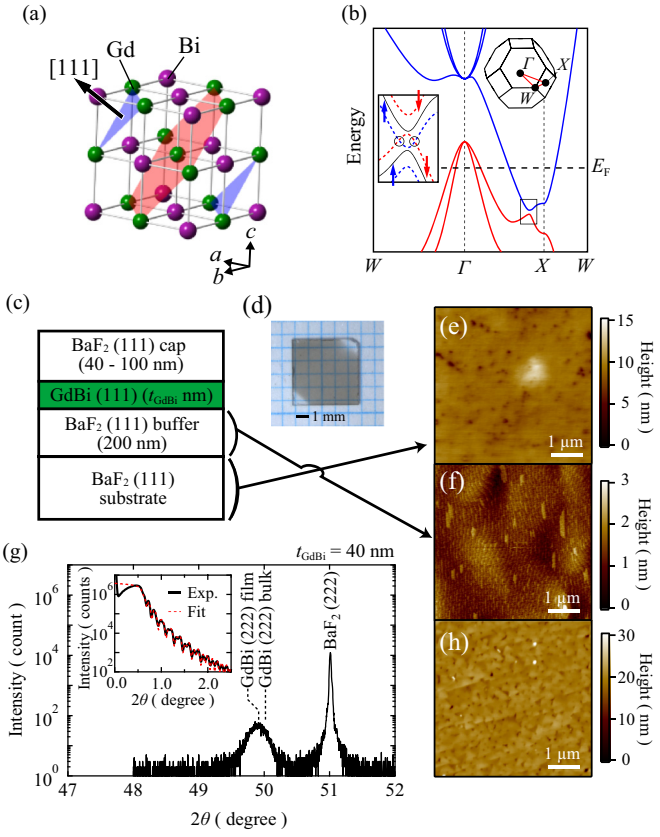

FIG. 1. Basic properties of GdBi thin films. (a) Crystal structure of antiferromagnetic GdBi. The shaded areas denote the (111) planes, where spins are ferromagnetically aligned. The spin orientations are opposite between the red and blue shaded areas. (b) Schematic band structure of GdBi. Red and blue curves denote the valence and conduction bands, respectively. The upper inset shows the Brillouin zone and high symmetry lines. The lower inset shows an expanded view of the band structure around conduction and valence band anticrossing. (c) Schematic sample structure. (d) Optical micrograph of the sample with $t_{GdBi} = 5$ nm. Atomic force microscope image of (e) the surface of an annealed BaF_2 (111) substrate and (f) the BaF_2 buffer layer. (g) X-ray diffraction spectrum of the GdBi thin film with $t_{GdBi} = 40$ nm. Inset: X-ray reflectivity spectrum of the GdBi thin film. The best fit of a simulated reflectivity spectrum to the experimental data is shown as the red dashed curve. (h) Atomic force microscope image of the surface of the GdBi thin film with the BaF_2 and AlN cap layers.

III. EXPERIMENTAL RESULTS

A. Structural characterization

The growth of single crystalline GdBi was confirmed by x-ray diffraction as shown in Fig. 1(g), where the peak at $2\theta = 49.90^\circ$ is identified as GdBi (222). A slight shift of this peak from the bulk reference position $2\theta_{ref} = 50.02^\circ$ implies an epitaxial lattice strain of approximately 0.2%. The AFM image [Fig. 1(h)] and the x-ray reflectivity (XRR) oscillations [Fig. 1(g) inset] confirm a smooth surface on the top BaF_2 and AlN cap layers. The thickness of the GdBi layer was calibrated by fitting the XRR oscillations to a model structure simulation [30].

B. Magnetic characterization

Figure 2(a) shows a comparison of the temperature T dependence of magnetic susceptibility χ_{bulk} of a GdBi bulk single crystal and the magnetic moment m of a 40-nm-thick GdBi thin film measured by a commercial superconducting quantum interference device (SQUID) magnetometer. The thin film was capped with an approximately 30 nm of AlN layer to prevent degradation of the magnetic properties. We confirmed that the magnetic properties of the thin-film samples stayed unchanged during the measurements. As previously reported [1,23], the bulk crystal exhibits an AFM transition with Neel temperature $T_N = 28$ K as identified by the kink in $\chi_{bulk}(T)$ (measured here with the applied field H parallel to [100]). While for the thin-film samples there is a relatively large background response arising from the substrate, buffer, and capping layers, there is a discernible peak for $T \sim T_N$ for H perpendicular to [111]. For H parallel to [111] this feature is largely suppressed, suggestive of the anisotropic magnetic susceptibility in the AFM phase.

To study the magnetic response of the films with higher resolution, we performed torque magnetometry experiments. As shown in the inset of Fig. 2(b), we mounted the sample directly to the end of a metal cantilever with a small angle $\theta \approx 15^\circ$ between the magnetic field and the sample normal. The magnetic torque $\tau(H)$ is shown in Fig. 2(b); at $T = 100$ K we observe a quadratic response typical of a paramagnetic susceptibility. This response is enhanced at $T = 30$ K while a prominent dip at intermediate H develops at the lowest

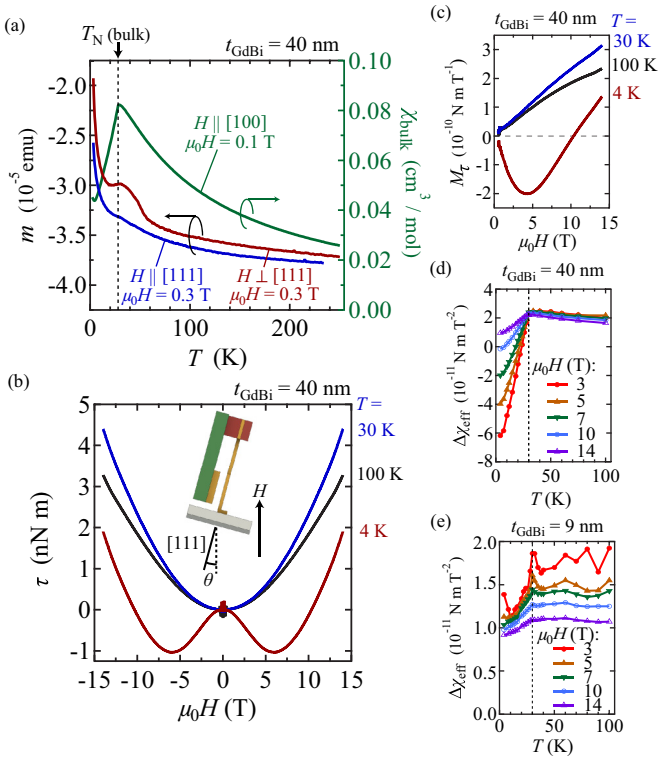

FIG. 2. Antiferromagnetic ordering in GdBi thin films. (a) Temperature dependence of the magnetic moment m for $t_{GdBi} = 40$ nm (red and blue curves, left axis) and magnetic susceptibility χ_{bulk} for a GdBi bulk single crystal (green curve, right axis) measured by a SQUID magnetometer with field orientations as indicated. (b) Magnetic field dependence of magnetic torque τ of the GdBi thin film sample ($t_{GdBi} = 40$ nm) grown on a 0.5-mm-thick BaF_2 substrate measured at different temperatures. The measurement geometry is shown in the inset. (c) Magnetic field dependence of torque magnetization M_τ at different temperatures. Magnetic field dependence of $\Delta\chi_{eff}$ calculated from M_τ for (d) $t_{GdBi} = 40$ nm and (e) $t_{GdBi} = 9$ nm as a function of temperature in various magnetic fields.

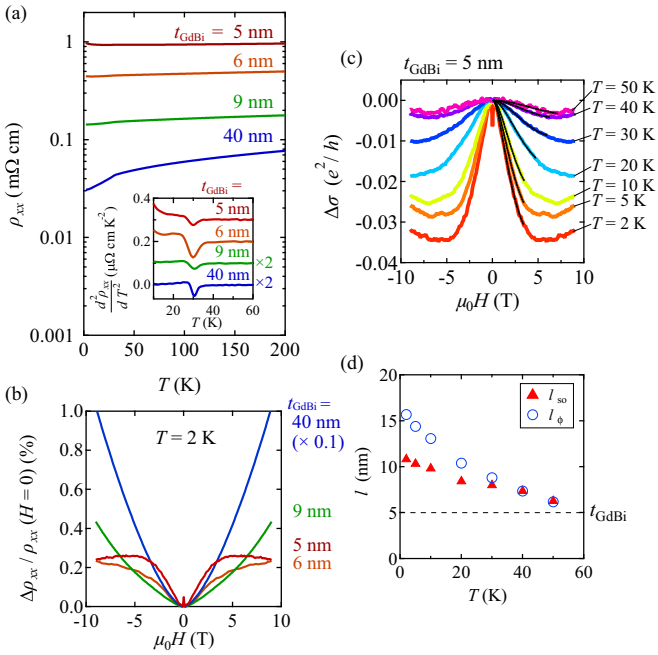

FIG. 3. Change of metallicity with the thickness of GdBi thin films. (a) Temperature dependence of longitudinal resistivity $\rho_{xx}(T)$ for various t_{GdBi}. Inset: Second derivative of $\rho_{xx}(T)$. Vertical offsets are added for clarity. (b) Magnetic field dependence of longitudinal resistivity $\rho_{xx}(H)$ measured at $T = 2$ K for various t_{GdBi}. $\Delta\rho_{xx} = \rho_{xx}(H) - \rho_{xx}(0)$. The data for $t_{GdBi} = 40$ nm are scaled by a factor of 0.1. (c) Modulation of conductivity by the magnetic fields at different temperatures for the 5-nm GdBi film. $\Delta\sigma = \sigma(H) - \sigma(0)$, where σ is the conductivity. Low field region of the data is fitted to the HLN theory and the best fits to the data are shown as thin black curves. (d) Temperature dependence of l_{SO} and l_ϕ extracted from the fitting.

$T = 4$ K. This is reminiscent of the W-shaped negative torque response originating from diamagnetism in superconducting states of high-T_c cuprates [31].

In Fig. 2(c) we plot the corresponding torque magnetization $M_\tau \equiv \tau/\mu_0 H = M_{plane} - M_{norm}$, where μ_0 is the vacuum permeability, M_{plane}, and M_{norm} are the magnetization parallel and normal to the sample plane, respectively. Here the trend of an approximately linear susceptibility giving way to a strong nonlinear response at low T can also be observed.

The nonlinear $M_\tau(H)$ at low T can be naturally explained by the development of magnetic anisotropy upon entering the AFM phase as observed in the SQUID measurements. In the absence of magnetic field, the GdBi thin film forms antiferromagnetic domains, and the Gd spins point to symmetrically equivalent directions. Therefore the susceptibility is nearly isotropic for $H \sim 0$. However, application of magnetic field $H < 5$ T flops the spins due to anisotropic susceptibility of an antiferromagnet, and confine them within the sample plane. In this configuration, the spin susceptibilities are anisotropic depending on magnetic field directions parallel or perpendicular to the sample plane. This generates the torque response as in Fig. 2(b) acted on by the tilted magnetic field.

As the anisotropy of the magnetic susceptibility develops in the AFM state, it can be used to probe the Neel temperature of the films T_N^{film}. We plot the observed anisotropy of effective magnetic susceptibility $\Delta\chi_{eff} \equiv \chi_{plane} - \chi_{norm} = M_\tau/\mu_0 H$ in Fig. 2(d) for different H and identify $T_N^{film} = 30$ K. The results for a thinner film with $t_{GdBi} = 9$ nm are shown in Fig. 2(e) where a similar T_N^{film} is observed.

C. Electrical characterization

The coupling between the conduction electrons and localized magnetic moments of GdBi allows further characterization of the magnetic transition using electrical transport. Figure 3(a) shows the T dependence of longitudinal resistivity $\rho_{xx}(T)$ for different t_{GdBi}. For the thickest film with $t_{GdBi} = 40$ nm we observe a metallic response for all T with a kink in $\rho_{xx}(T)$ near $T = 30$ K, the latter more clearly observed in the second derivative $d^2\rho_{xx}/dT^2$ shown in the inset of Fig. 3(a). At all thicknesses down to $t_{GdBi} = 5$ nm we observe this kink near $T = 30$ K. This approximately matches the observed T_N^{film} shown in Figs. 2(d) and 2(e), suggesting that it is associated with the AFM transition. Such a $\rho_{xx}(T)$ feature has been previously reported in GdBi bulk single crystals and ascribed to suppressed spin disorder scattering in the AFM

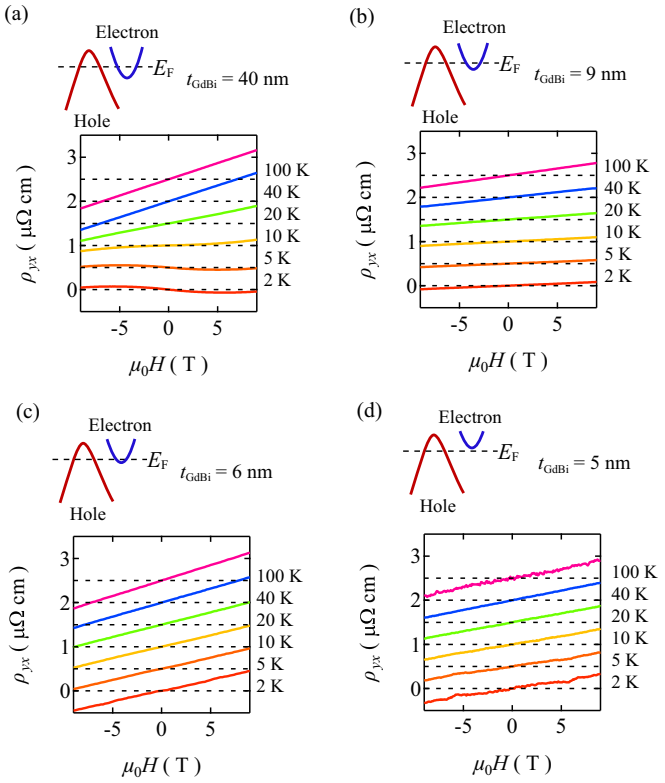

FIG. 4. Evolution of Hall effect as a function of GdBi film thickness. Transverse resistivity ρ_{yx} as a function of magnetic field at various temperatures for (a) $t_{GdBi} = 40$ nm, (b) $t_{GdBi} = 9$ nm, (c) $t_{GdBi} = 6$ nm, and (d) $t_{GdBi} = 5$ nm. The traces are offset vertically for clarity. The upper inset in each panel is a schematic depiction of the overlapping bulk bands.

phase [32]. The observation of this feature in $d^2\rho_{xx}/dT^2$ for all films down to $t_{GdBi} = 5$ nm therefore suggests that T_N^{film} remains unchanged down to at least five crystallographic unit cells of GdBi. As can be seen in Fig. 3(a), the overall electrical response of the films changes from metallic to nonmetallic with decreasing t_{GdBi}; the low T slope $d\rho_{xx}/dT$ changes from positive for $t_{GdBi} = 40$ nm to negative for $t_{GdBi} = 5$ nm. This suggests a possible shift of the bulk band edges in the system with decreasing t_{GdBi}, which we address further below.

The magnetotransport response of this series of films at $T = 2$ K is shown in Fig. 3(b), where a nonsaturating $[\rho_{xx}(H) - \rho_{xx}(H = 0)]/\rho_{xx}(H = 0)$ of approximately 10% at $\mu_0 H = 9$ T for the thickest films gives way to smaller, saturating behavior for thinner films. Bulk single crystals of GdBi and other *RX* systems have been reported to show extreme magnetoresistance (XMR) [23,33–36] of similar form to that seen here for the thickest films, but with significantly larger amplitude in the bulk case. As we discuss below, since XMR is influenced by band parameters including carrier density, mobility, and position of chemical potential [33], the qualitative change of this response in the thin limit probes the evolution of these parameters as well as the band structure itself.

To further investigate the t_{GdBi} dependence of transport, we measured the transverse (Hall) resistivity $\rho_{yx}(H)$ across a broad range of T. As shown in Fig. 4(a), for $t_{GdBi} = 40$ nm at $T = 2$ K we observe a nonlinear $\rho_{yx}(H)$ consistent with that expected from a semimetallic band structure. With decreasing t_{GdBi} [Figs. 4(b) to 4(d)], a linear response emerges suggestive of hole-like single-band transport. At elevated T, $\rho_{yx}(H)$ for thicker films ($t_{GdBi} \geqslant 9$ nm) evolves towards a linear response whereas for thinner films ($t_{GdBi} \leqslant 6$ nm) it remains unchanged.

IV. THEORETICAL INVESTIGATION

A. First-principles calculations

The electrical transport and the torque data in GdBi films suggest suppressed metallicity in the thin limit, while long-range magnetic correlation is unaffected. Experimentally achievable thickness of the GdBi films is thus far bounded by 5 nm or above and we were unable to achieve the regime where the nontrivial topology which GdBi may hold would manifest itself in the transport properties. Nevertheless, here we show by theoretical studies that GdBi has a topologically nontrivial band structure in both bulk and thin-film limits and exhibits Chern insulating state with $C = 2$ in monolayer limit.

We performed first-principles calculations of the electronic structures of bulk and ultrathin GdBi (111) in the type-II AFM phase [30]. The calculated bulk band structure is consistent with previous calculations [37,38]. Figure 5(a) shows the calculated band structure of bulk GdBi (111) with type-II AFM order in the hexagonal unit cell with spin-orbit coupling (SOC). It exhibits an indirect negative band gap of about -1 eV between the Bi-derived valence band at Γ-point and the Gd-derived conduction band at M points, forming a semimetal. From the systematic dependence of the calculated band structure as a function of the lattice constant, we confirmed that the bands are inverted at the M points. We also calculated the surface states and find they connect the bulk valence bands and conduction bands. All calculations confirm that bulk GdBi has a nontrivial band topology corresponding to an AFM topological insulator gap degenerate with trivial bulk electronic states.

In the ultrathin limit, monolayer GdBi (111) consists of a pair of single atomic layers of Gd and Bi, separated by lattice spacing d_1 from each other [Fig. 5(b)]. To determine the topology of GdBi (111) in the 2D limit, the band structure of monolayer GdBi (111) slab was calculated using $d_1 = 0.182$ nm (the bulk value) as shown in Fig. 5(c). We observe that the size of the negative indirect band gap is nearly lifted owing to the quantum confinement. The orbital-projection analysis reveals band inversion between the Gd d_{z^2} orbital and Bi p_x orbital at the $\overline{\Gamma}$ point, implying a nontrivial band topology.

B. Symmetry analysis and edge modes

To determine the topological properties relevant to monolayer GdBi (111), we performed symmetry analysis of the low energy band structure. Monolayer GdBi (111) has three-fold rotation symmetry C_3. Due to the magnetic order, both time-reversal symmetry T and mirror symmetry with the mirror plane perpendicular to y-direction M_y are broken, but the combined TM_y is preserved. To characterize the low-energy properties near $\overline{\Gamma}$, we use the little group containing C_3 and

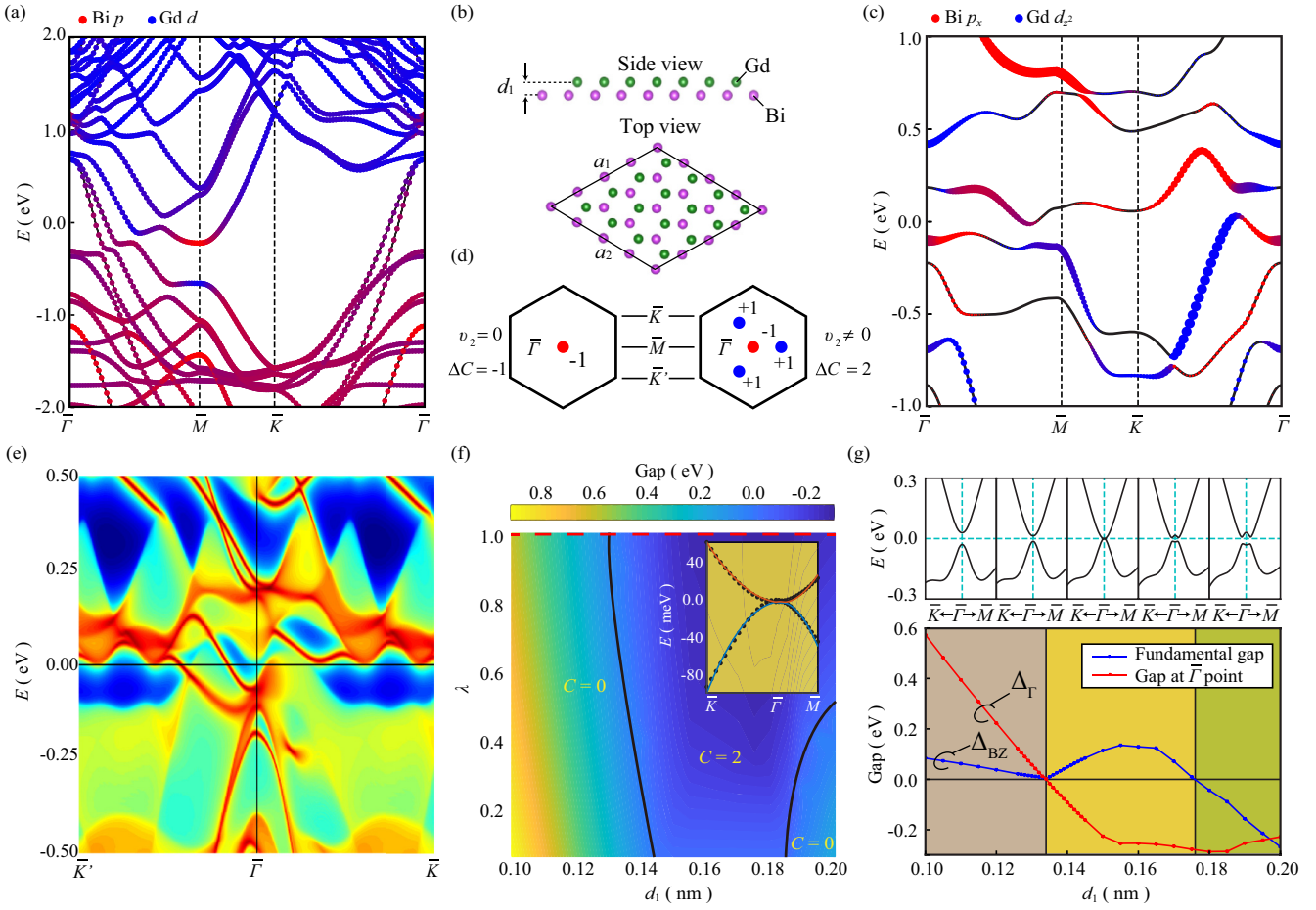

FIG. 5. Calculations of the GdBi band structure. (a) Band structure of bulk GdBi (111) with SOC. (b) Illustrated crystal structure of the monolayer GdBi (111). d_1 is the distance between Bi and Gd layers and a_1, a_2 are the in-plane lattice constants. (c) Typical band structure of the monolayer GdBi (111). (d) Schematic Brillouin zone of the monolayer GdBi (111). Color of the circle denotes the change in the Chern number ΔC across the topological phase transition, contributed by each Dirac point: red for -1 and blue for $+1$. (e) Edge states of monolayer GdBi (111) along zigzag direction, exhibiting a pair of edge modes around the $\bar{\Gamma}$ point. (f) Topological phase diagram of monolayer GdBi (111) as functions of d_1 and SOC strength λ. The color represents the direct gap size and negative value indicates inverted band ordering. Inset: Fit results of $k \cdot p$ model band structure (solid line) to the first-principles calculations (empty circle) for $d_1 = 0.134$ nm. (g) Strain induced topological phase transition of the monolayer GdBi (111). Top panel: Evolution of monolayer GdBi band structure as a function of d_1. Bottom panel: Direct gap Δ_Γ at the $\bar{\Gamma}$ point (red line) and the fundamental gap Δ_{BZ} across the Brillouin zone (blue line) as a function of d_1. System is a Chern insulator with $C = 2$ when $\Delta_\Gamma < 0$, and is semimetallic when $\Delta_{BZ} < 0$.

TM_y symmetries to build a $k \cdot p$ Hamiltonian

$$H(k_x, k_y) = m_1\sigma_z + m_2\left(k_x^2 + k_y^2\right)\sigma_z + v_1(k_x\sigma_y - k_y\sigma_x) + v_2\left(2k_xk_y\sigma_y - \left(k_x^2 - k_y^2\right)\sigma_x\right) + v_3\left(k_x^2 + k_y^2\right)I, \quad (1)$$

where σ is the pseudospin representing the conduction and valence bands, m_1 and m_2 are mass parameters, k_x and k_y are the crystal momenta, and v_1, v_2, and v_3 are the velocity parameters. The v_3 term gives the same energy shift for both conduction and valence bands and thus will not affect the topological properties. We therefore set $v_3 = 0$ in the following.

For the simplest case with $m_2 = v_2 = 0$, the $k \cdot p$ Hamiltonian reduces to the typical massive Dirac Hamiltonian. For $m_1 \neq 0$, a gap will open at $\bar{\Gamma}$ [red circles in Fig. 5(d)]. Across this band inversion, a topological phase transition occurs with Chern number changed by $\Delta C = -1$. In the case of small $v_2 \neq 0$, Dirac cones appear at four different points: one at $\bar{\Gamma}$ and the other three at equivalent points along the $\bar{\Gamma} - \bar{M}$ lines [blue circles in Fig. 5(d)]. As m_1 changes from negative to positive, the total Chern number now changes by $\Delta C = 2$. For $v_2 \gg v_1$, as v_2 increases the three Dirac points along the $\bar{\Gamma} - \bar{M}$ line converge at $\bar{\Gamma}$ and transform into a quadratic band touching. As in the case of small v_2, $\Delta C = 2$ when m_1 changes sign. For $m_2 \neq 0$, $m_2(k_x^2 + k_y^2) = 0$ at $\bar{\Gamma}$ and m_2 will not affect the gap closing or reopening there. However, m_2 does affect the gap along the $\bar{\Gamma} - \bar{M}$ lines. By fine-tuning m_2, we can also realize an intermediate phase with $C = -1$ or 3 between $C = 0$ and $C = 2$ phases; the parameter regime of the intermediate phase is $\delta = |m_2|(\frac{v_1}{v_2})^2$.

To confirm the Chern insulating state with $C = 2$, we show in Fig. 5(e) the edge states along zigzag direction, which are calculated in *ab initio* tight-binding models with all the parameters fitted from the first-principles calculations

through WANNIER90 [39]. It shows two chiral edge modes connecting the valence and the conduction bands around the $\overline{\Gamma}$ point. These modes always appear as a pair, reflecting the topological band character $C = 2$.

C. Calculations of topological phase transition

We performed systematic calculations for the topological phase diagram for monolayer GdBi by varying the interlayer distance d_1 and the SOC strength λ. As shown in Fig. 5(f), the phase diagram contains only phases with $C = 0$ and $C = 2$. As shown in the top panel of Fig. 5(g), the conduction band and valence band have quadratic touching at the band inversion (similar behavior happens when we vary SOC strength λ as shown in Supplemental Material [30]), which indicates a high-order topological phase transition. Fitting all the parameters in the $k \cdot p$ model to the band structures around the critical distance $d = 1.34$ [inset of Fig. 5(f)], we find $v_1 = -0.3$, $v_2 = 37.2$, $v_3 = -7.1$, and $|m_2| < 0.1$. This is consistent with the phase diagram obtained by first-principles calculations (the intermediate phase $\delta = |m_2|(\frac{v_1}{v_2})^2 \sim 10^{-5}$ is extremely small). In Fig. 5(g), we show the evolution of the energy gap Δ at the $\overline{\Gamma}$ point as a function of d_1. Δ monotonically decreases when d_1 increases for $d_1 < 0.134$ nm. At $d_1 = 0.134$, $\Delta = 0$ and the gap reopens for $d_1 > 0.134$ nm indicating a topological phase transition.

V. DISCUSSION

The GdBi thin films studied here appear to retain the magnetic properties of bulk crystals down to $t_{\mathrm{GdBi}} = 5$ nm, suggesting that the symmetry breaking AFM order of these materials is not significantly altered. The transport response, on the other hand, does evolve significantly on decreasing thickness particularly across $t_{\mathrm{GdBi}} = 9$ nm. By quantitatively analyzing the magnetotransport results, we can connect this behavior with that reported for bulk single crystals as well as that predicted by our theoretical calculations in the thin limit.

Starting with the thickest film with $t_{\mathrm{GdBi}} = 40$ nm, we expect a minimal role of quantum confinement and therefore transport behavior similar to bulk single crystal materials. While we do observe a nonsaturating magnetoresistivity [Fig. 3(b)], the overall magnitude of this response is significantly smaller than the XMR behavior reported in bulk single crystals [35]. This can be understood in terms of the compensation model for XMR which requires a balance of density and mobility of the conduction and valence bands [40,41]. While compensation has been observed in bulk *RX* systems [23,29,34,36,42–44], two band analysis [30] of the magnetotransport results for our $t_{\mathrm{GdBi}} = 40$ nm film [Fig. 4(a)] yields $n_e = 2.5 \times 10^{20}$ cm^{-2}, $n_h = 3.0 \times 10^{20}$ cm^{-2}, $\mu_e = 389$ cm^2/Vs, $\mu_h = 349$ cm^2/Vs for $t_{\mathrm{GdBi}} = 40$ nm at $T = 2$ K, where n_e, n_h, μ_e, and μ_h are the electron density, the total hole density, the electron mobility, and the hole mobility, respectively. While the carrier densities are similar to those observed in bulk GdBi, along with reduced overall mobility they are detuned enough from perfect compensation to explain the significantly reduced XMR response [45–47]. The origin of this difference of parameters could arise from a number of sources including charge transfer from the substrate, defect chemistry differences in bulk and thin film synthesis, or epitaxial strain.

Upon decreasing t_{GdBi}, the compensation is further removed such that by $t_{\mathrm{GdBi}} = 6$ nm the $T = 2$ K Hall effect is captured by a purely hole-like $\rho_{yx}(H)$ [see Fig. 4(c)]. A plausible explanation for this is a confinement-induced [22,48] upward shifting of the electron band. This scenario is depicted schematically in the upper insets of Figs. 4(a) to 4(d) and corresponds to a decrease of the semimetallic band overlap at E_F. This is further consistent with the change from metallic to mildly insulating behavior in $\rho_{xx}(T)$ shown in Fig. 3(a): here the hole-like bands remain metallic but the upwards shifted electron band has a parallel thermally activated conductivity with a relatively minor contribution to the off-diagonal response.

We find that magnetoresistance in the 5- and 6-nm films quickly increases in low field regions, while the 9- and 40-nm films are dominated by the quadratic orbital magnetoresistance. The features of the 5- and 6-nm data can be understood in terms of weak antilocalization. According to the Hikami-Larkin-Nagaoka (HLN) theory, correction of conductivity due to weak antilocalization is given by [49]

$$\begin{aligned}\frac{\Delta\sigma}{(e^2/\pi h)} &= \ln\left(\frac{H}{H_{\mathrm{SO}}+H_\phi}\right) + \psi\left(\frac{1}{2}+\frac{H_{\mathrm{SO}}+H_\phi}{H}\right) \\ &\quad - \frac{1}{2}\ln\left(\frac{H}{H_\phi}\right) - \frac{1}{2}\psi\left(\frac{1}{2}+\frac{H_\phi}{H}\right) \\ &\quad + \frac{1}{2}\ln\left(\frac{H}{2H_{\mathrm{SO}}+H_\phi}\right) \\ &\quad + \frac{1}{2}\psi\left(\frac{1}{2}+\frac{2H_{\mathrm{SO}}+H_\phi}{H}\right), \end{aligned} \tag{2}$$

assuming spin-flip scattering is negligible and the electron diffusive regime, where e and h are the electron charge and Planck's constant, respectively, H_{SO}, and H_ϕ are the characteristic fields for spin-orbit scattering and phase coherence, respectively, and ψ is the digamma function. The fit results of this formula to the magnetoconductivity data is shown in Fig. 3(c). It shows reasonable agreement with the experimental data in low-field regions, and gives the characteristic lengths for spin-orbit scattering $l_{\mathrm{SO}} = (\hbar/4e\mu_0 H_{\mathrm{SO}})^{1/2}$ and phase coherence length $l_\phi = (\hbar/4e\mu_0 H_\phi)^{1/2}$ as plotted in Fig. 3(d), where $\hbar$ and μ_0 are the reduced Planck's constant and vacuum permeability, respectively. We find l_{SO} and l_ϕ are larger than the film thickness, justifying the use of HLN theory in the two-dimensional limit. We see that the phase coherence length increases rapidly below the Neel temperature of GdBi thin films $T_N = 30$ K stemming from the suppressed scattering by magnetic fluctuations. The spin-orbit scattering dominates the scattering in this regime. As the effect of weak antilocalization is generally enhanced in the low-dimensional limit, the observation of the features only in our thinnest films supports the evidence that they are approaching the two-dimensional limit.

Stabilizing films with further reduced t_{GdBi} would then be expected to further enhance quantum confinement toward the realization of the $C = 2$ Chern insulator state as predicted in our *ab initio* calculations. We anticipate that in the ultrathin limit Anderson localization is also relevant [50]; this will act

to eventually gap out the nontrivial electronic states, and in the case of a time-reversal symmetry breaking by canting of the AFM order, potentially isolate chiral modes across a broad energy range [51]. We expect that the metal-to-insulator transition can also be driven by the lattice strain from the substrate. Considering that BaF_2 is a relatively well-lattice-matched substrate and the large negative band gap of bulk GdBi, we expect the quantum confinement is playing a dominant role for lifting semimetallicity as was seen in thin films of other semimetallic systems [52]. The effect of strain, however, is expected to play important roles in determining electronic properties in a few-layer films.

Analyzing our theoretical calculations offers insight into the underlying mechanism by which monolayer GdBi may realize a $C = 2$ phase. This appears to be a result of the collapse of the intermediate phase corresponding to more conventional $\Delta C = 1$ transitions found when $|m_2|$ is small and v_2 is very large (and further that this is the physically relevant regime for monolayer GdBi). This approach to realizing the $C = 2$ Chern insulating state is general and may be relevant to the recently proposed $C = 2$ state in the Dice lattice with C_{3v} symmetry [53] and also to the topological crystalline insulator SnTe with the mirror Chern number 2 [54]. Our further demonstration that this phase is sensitive to the layer spacing parameter d_1 suggests the opportunity to engineer band topology using lattice strain, which can be controlled either by external pressure or by epitaxial strain [55]. Therefore monolayer GdBi (111) is an attractive system to realize a tunable $C = 2$ Chern insulator state.

VI. CONCLUSION

We report the structural, magnetic, and transport properties of the correlated topological insulator candidate GdBi thin films. We find bringing materials to the thin-film limit preserves the antiferromagnetic properties of bulk single crystals but with modified electrical properties consistent with a lifting of the semimetallic band overlap. Together with our first-principles calculations that show the band topology is preserved in the monolayer limit, this demonstrates that GdBi and other magnetic *RX* systems in thin film form are candidates for hosting intrinsic correlated topological phases, including antiferromagnetic TIs [13], and $C = 2$ Chern insulating phase tunable by strain in the monolayer limit [15,56–58].

Although experimentally accessible thickness thus far is limited above five crystallographic unit cells, stabilization of GdBi in thin film form is a step toward realizing the high Chern number insulator in a real material. We expect that by further optimizing growth conditions and combining with *in-situ* spectroscopic measurements, characterization of GdBi near the monolayer limit is possible as recently demonstrated in an another topologically nontrivial system [59]. Tuning electronic properties of GdBi thin films by strain, electrostatic gating, or chemical doping would be other important directions of research and would corroborate the topologically nontrivial properties of this material.

We also note that the films here have a (111) orientation that has thus far not been stabilized for spectroscopic studies in bulk single crystals [2,4–6,8,9,29]. Theoretical calculations for *R*Bi predict that three surface Dirac cones are each separately projected on to distinct points in the Brillouin zones on the (111) surface, but that two are degenerate and obscured by bulk bands for the (currently available) (001) surface [3]. Therefore, the high quality (111)-oriented films reported here even in the thick limit may serve an important role for improved spectroscopic characterization. Finally, following the methodology presented herein, we expect that other members of the *RX* family with more complex magnetic phase diagrams including CeBi [60] and HoBi [61,62] should also be readily synthesized, allowing for exploration of a wide variety of novel symmetry broken phases in this new class of topological electronic materials.

ACKNOWLEDGMENTS

We are grateful to L. Fu and C. Fang for fruitful discussions. This research was funded, in part, by the Gordon and Betty Moore Foundation EPiQS Initiative, Grant No. GBMF3848 to J.G.C. and ARO Grant No. W911NF-16-1-0034. J.G.C. acknowledges support from the Bose Fellows Program at MIT. M. Hu and J. Liu acknowledge financial support from the Hong Kong Research Grants Council (Project No. ECS26302118). The authors acknowledge characterization facility support provided by the Materials Research Laboratory at Massachusetts Institute of Technology, as well as fabrication facility support by the Microsystems Technology Laboratories at Massachusetts Institute of Technology. H. Inoue, M. Han, and M. Hu contributed equally to this work.

[1] C.-G. Duan, R. F. Sabirianov, W. N. Mei, P. A. Dowben, S. S. Jaswal, and E. Y. Tsymbal, Electronic, magnetic and transport properties of rare-earth monopnictides, J. Phys.: Condens. Matter **19**, 315220 (2007).

[2] Y. Wu, Y. Lee, T. Kong, D. Mou, R. Jiang, L. Huang, S. L. Bud'Ko, P. C. Canfield, and A. Kaminski, Electronic structure of *R*Sb (R = Y, Ce, Gd, Dy, Ho, Tm, Lu) studied by angle-resolved photoemission spectroscopy, Phys. Rev. B **96**, 035134 (2017).

[3] M. Zeng, C. Fang, G. Chang, Y.-A. Chen, T. Hsieh, A. Bansil, H. Lin, and L. Fu, Topological semimetals and topological insulators in rare earth monopnictides, arXiv:1504.03492.

[4] J. Nayak, S.-C. Wu, N. Kumar, C. Shekhar, S. Singh, J. Fink, E. E. D. Rienks, G. H. Fecher, S. S. P. Parkin, B. Yan, and C. Felser, Multiple Dirac cones at the surface of the topological metal LaBi, Nat. Commun. **8**, 13942 (2017).

[5] R. Lou, B. B. Fu, Q. N. Xu, P. J. Guo, L. Y. Kong, L. K. Zeng, J. Z. Ma, P. Richard, C. Fang, Y. B. Huang, S. S. Sun, Q. Wang, L. Wang, Y. G. Shi, H. C. Lei, K. Liu, H. M. Weng, T. Qian, H. Ding, and S. C. Wang, Evidence of topological insulator state in the semimetal LaBi, Phys. Rev. B **95**, 115140 (2017).

[6] B. Feng, J. Cao, M. Yang, Y. Feng, S. Wu, B. Fu, M. Arita, K. Miyamoto, S. He, K. Shimada, Y. Shi, T. Okuda, and Y.

Yao, Experimental observation of node-line-like surface states in LaBi, Phys. Rev. B **97**, 155153 (2018).

[7] X. Duan, F. Wu, J. Chen, P. Zhang, Y. Liu, H. Yuan, and C. Cao, Tunable electronic structure and topological properties of LnPn (Ln = Ce, Pr, Sm, Gd, Yb; Pn = Sb, Bi), Commun. Phys. **1**, 71 (2018).

[8] K. Kuroda, M. Ochi, H. S. Suzuki, M. Hirayama, M. Nakayama, R. Noguchi, C. Bareille, S. Akebi, S. Kunisada, T. Muro, M. D. Watson, H. Kitazawa, Y. Haga, T. K. Kim, M. Hoesch, S. Shin, R. Arita, and T. Kondo, Experimental Determination of the Topological Phase Diagram in Cerium Monopnictides, Phys. Rev. Lett. **120**, 086402 (2018).

[9] N. Alidoust, A. Alexandradinata, S.-Y. Xu, I. Belopolski, S. K. Kushwaha, M. Zeng, M. Neupane, G. Bian, C. Liu, D. S. Sanchez, P. P. Shibayev, H. Zheng, L. Fu, A. Bansil, H. Lin, R. J. Cava, and M. Z. Hasan, A new form of (unexpected) Dirac fermions in the strongly-correlated cerium monopnictides, arXiv:1604.08571.

[10] C. L. Kane and E. J. Mele, Z_2 Topological Order and the Quantum Spin Hall Effect, Phys. Rev. Lett. **95**, 146802 (2005).

[11] X. L. Qi and S. C. Zhang, Topological insulators and superconductors, Rev. Mod. Phys. **83**, 1057 (2011).

[12] B. A. Bernevig and S.-C. Zhang, Quantum Spin Hall Effect, Phys. Rev. Lett. **96**, 106802 (2006).

[13] R. S. K. Mong, A. M. Essin, and J. E. Moore, Antiferromagnetic topological insulators, Phys. Rev. B **81**, 245209 (2010).

[14] C.-X. Liu, S.-C. Zhang, and X.-L. Qi, The quantum anomalous Hall effect: Theory and experiment, Annu. Rev. Condens. Matter Phys. **7**, 301 (2016).

[15] C.-Z. Chang, J. Zhang, X. Feng, J. Shen, Z. Zhang, M. Guo, K. Li, Y. Ou, P. Wei, L.-L. Wang, Z.-Q. Ji, Y. Feng, S. Ji, X. Chen, J. Jia, X. Dai, Z. Fang, S.-C. Zhang, K. He, Y. Wang, L. Lu, X.-C. Ma, and Q.-K. Xue, Experimental observation of the quantum anomalous Hall effect in a magnetic topological insulator, Science **340**, 167 (2013).

[16] M. Winnerlein, S. Schreyeck, S. Grauer, S. Rosenberger, K. M. Fijalkowski, C. Gould, K. Brunner, and L. W. Molenkamp, Epitaxy and structural properties of $(V, Bi, Sb)_2Te_3$ layers exhibiting the quantum anomalous Hall effect, Phys. Rev. Mater. **1**, 011201(R) (2017).

[17] C. X. Liu, X. L. Qi, X. Dai, Z. Fang, and S. C. Zhang, Quantum Anomalous Hall Effect in $Hg_{1-y}Mn_yTe$ Quantum Wells, Phys. Rev. Lett. **101**, 146802 (2008).

[18] Y. Zhang, K. He, C.-Z. Chang, C.-L. Song, L.-L. Wang, X. Chen, J.-F. Jia, Z. Fang, X. Dai, W.-Y. Shan, S.-Q. Shen, Q. Niu, X.-L. Qi, S.-C. Zhang, X.-C. Ma, and Q.-K. Xue, Crossover of the three-dimensional topological insulator Bi_2Se_3 to the two-dimensional limit, Nat. Phys. **6**, 584 (2010).

[19] J. Zhang, C.-Z. Chang, Z. Zhang, J. Wen, X. Feng, K. Li, M. Liu, K. He, L. Wang, X. Chen, Q.-K. Xue, X. Ma, and Y. Wang, Band structure engineering in $(Bi_{1-x}Sb_x)_2Te_3$ ternary topological insulators, Nat. Commun. **2**, 574 (2011).

[20] J. G. Checkelsky, Y. S. Hor, R. J. Cava, and N. P. Ong, Bulk Band Gap and Surface State Conduction Observed in Voltage-Tuned Crystals of the Topological Insulator Bi_2Se_3, Phys. Rev. Lett. **106**, 196801 (2011).

[21] Y.-Y. Li, G. Wang, X.-G. Zhu, M.-H. Liu, C. Ye, X. Chen, Y.-Y. Wang, K. He, L.-L. Wang, X.-C. Ma, H.-J. Zhang, X. Dai, Z. Fang, X.-C. Xie, Y. Liu, X.-L. Qi, J.-F. Jia, S.-C. Zhang, and Q.-K. Xue, Intrinsic topological insulator Bi_2Te_3 thin films on Si and their thickness limit, Adv. Mater. **22**, 4002 (2010).

[22] Z. Li, J. Kim, N. Kioussis, S. Y. Ning, H. Su, T. Iitaka, T. Tohyama, X. Yang, and J. X. Zhang, GdN thin film: Chern insulating state on square lattice, Phys. Rev. B **92**, 201303(R) (2015).

[23] L. Ye, T. Suzuki, C. R. Wicker, and J. G. Checkelsky, Extreme magnetoresistance in magnetic rare-earth monopnictides, Phys. Rev. B **97**, 081108(R) (2018).

[24] C.-G. Duan, R. F. Sabiryanov, W. N. Mei, P. A. Dowben, S. S. Jaswal, and E. Y. Tsymbal, Magnetic ordering in Gd monopnictides: Indirect exchange versus superexchange interaction, Appl. Phys. Lett. **88**, 182505 (2006).

[25] M. Hirschberger, S. Kushwaha, Z. Wang, Q. Gibson, S. Liang, C. A. Belvin, B. A. Bernevig, R. J. Cava, and N. P. Ong, The chiral anomaly and thermopower of Weyl fermions in the half-Heusler GdPtBi, Nat. Mater. **15**, 1161 (2016).

[26] T. Suzuki, R. Chisnell, A. Devarakonda, Y. T. Liu, W. Feng, D. Xiao, J. W. Lynn, and J. G. Checkelsky, Large anomalous Hall effect in a half-Heusler antiferromagnet, Nat. Phys. **12**, 1119 (2016).

[27] J. Cano, B. Bradlyn, Z. Wang, M. Hirschberger, N. P. Ong, and B. A. Bernevig, Chiral anomaly factory: Creating Weyl fermions with a magnetic field, Phys. Rev. B **95**, 161306(R) (2017).

[28] N. P. Armitage, E. J. Mele, and A. Vishwanath, Weyl and Dirac semimetals in three-dimensional solids, Rev. Mod. Phys. **90**, 015001 (2018).

[29] L.-K. Zeng, R. Lou, D.-S. Wu, Q. N. Xu, P.-J. Guo, L.-Y. Kong, Y.-G. Zhong, J.-Z. Ma, B.-B. Fu, P. Richard, P. Wang, G. T. Liu, L. Lu, Y.-B. Huang, C. Fang, S.-S. Sun, Q. Wang, L. Wang, Y.-G. Shi, H. M. Weng, H.-C. Lei, K. Liu, S.-C. Wang, T. Qian, J.-L. Luo, and H. Ding, Compensated Semimetal LaSb with Unsaturated Magnetoresistance, Phys. Rev. Lett. **117**, 127204 (2016).

[30] See Supplemental Material at http://link.aps.org/supplemental/10.1103/PhysRevMaterials.3.101202 for more information.

[31] Y. Wang, L. Li, M. J. Naughton, G. D. Gu, S. Uchida, and N. P. Ong, Field-Enhanced Diamagnetism in the Pseudogap State of the Cuprate $Bi_2Sr_2CaCu_2O_{8+\delta}$ Superconductor in an Intense Magnetic Field, Phys. Rev. Lett. **95**, 247002 (2005).

[32] D. X. Li, Y. Haga, H. Shida, T. Suzuki, and Y. S. Kwon, Electrical transport properties of semimetallic GdX single crystals (X = P, As, Sb, and Bi), Phys. Rev. B **54**, 10483 (1996).

[33] N. Kumar, C. Shekhar, S.-C. Wu, I. Leermakers, O. Young, U. Zeitler, B. Yan, and C. Felser, Observation of pseudo-two-dimensional electron transport in the rock salt-type topological semimetal LaBi, Phys. Rev. B **93**, 241106(R) (2016).

[34] F. F. Tafti, Q. Gibson, S. Kushwaha, J. W. Krizan, N. Haldolaarachchige, and R. J. Cava, Temperature-field phase diagram of extreme magnetoresistance, Proc. Natl. Acad. Sci. USA **113**, E3475 (2016).

[35] F. F. Tafti, Q. D. Gibson, S. K. Kushwaha, N. Haldolaarachchige, and R. J. Cava, Resistivity plateau and extreme magnetoresistance in LaSb, Nat. Phys. **12**, 272 (2016).

[36] F. Han, J. Xu, A. S. Botana, Z. L. Xiao, Y. L. Wang, W. G. Yang, D. Y. Chung, M. G. Kanatzidis, M. R. Norman, G. W. Crabtree, and W. K. Kwok, Separation of electron and hole dynamics in the semimetal LaSb, Phys. Rev. B **96**, 125112 (2017).

[37] P. Larson and W. R. L. Lambrecht, Electronic structure of Gd pnictides calculated within the LSDA+U approach, Phys. Rev. B **74**, 085108 (2006).

[38] R. Masrour, E. K. Hlil, M. Hamedoun, and A. Benyoussef, Investigation of electronic and magnetic properties of antiferromagnetic GdBi system by first principle and series expansions calculations, Comput. Mater. Sci. **84**, 45 (2014).

[39] A. A. Mostofi, J. R. Yates, G. Pizzi, Y.-S. Lee, I. Souza, D. Vanderbilt, and N. Marzari, An updated version of wannier90: A tool for obtaining maximally-localised Wannier functions, Comput. Phys. Commun. **185**, 2309 (2014).

[40] M. N. Ali, J. Xiong, S. Flynn, J. Tao, Q. D. Gibson, L. M. Schoop, T. Liang, N. Haldolaarachchige, M. Hirschberger, N. P. Ong, and R. J. Cava, Large, non-saturating magnetoresistance in WTe_2, Nature **514**, 205 (2014).

[41] C. Shekhar, A. K. Nayak, Y. Sun, M. Schmidt, M. Nicklas, I. Leermakers, U. Zeitler, Y. Skourski, J. Wosnitza, Z. Liu, Y. Chen, W. Schnelle, H. Borrmann, Y. Grin, C. Felser, and B. Yan, Extremely large magnetoresistance and ultrahigh mobility in the topological Weyl semimetal candidate NbP, Nat. Phys. **11**, 645 (2015).

[42] P.-J. Guo, H.-C. Yang, B.-J. Zhang, K. Liu, and Z.-Y. Lu, Charge compensation in extremely large magnetoresistance materials LaSb and LaBi revealed by first-principles calculations, Phys. Rev. B **93**, 235142 (2016).

[43] J. He, C. Zhang, N. J. Ghimire, T. Liang, C. Jia, J. Jiang, S. Tang, S. Chen, Y. He, S.-K. Mo, C. C. Hwang, M. Hashimoto, D. H. Lu, B. Moritz, T. P. Devereaux, Y. L. Chen, J. F. Mitchell, and Z.-X. Shen, Distinct Electronic Structure for the Extreme Magnetoresistance in YSb, Phys. Rev. Lett. **117**, 267201 (2016).

[44] N. Wakeham, E. D. Bauer, M. Neupane, and F. Ronning, Large magnetoresistance in the antiferromagnetic semimetal NdSb, Phys. Rev. B **93**, 205152 (2016).

[45] L. Wang, I. Gutiérrez-Lezama, C. Barreteau, N. Ubrig, E. Giannini, and A. F. Morpurgo, Tuning magnetotransport in a compensated semimetal at the atomic scale, Nat. Commun. **6**, 8892 (2015).

[46] F. F. Tafti, M. S. Torikachvili, R. L. Stillwell, B. Baer, E. Stavrou, S. T. Weir, Y. K. Vohra, H.-Y. Yang, E. F. McDonnell, S. K. Kushwaha, Q. D. Gibson, R. J. Cava, and J. R. Jeffries, Tuning the electronic and the crystalline structure of LaBi by pressure: From extreme magnetoresistance to superconductivity, Phys. Rev. B **95**, 014507 (2017).

[47] S. Sun, Q. Wang, P. J. Guo, K. Liu, and H. Lei, Large magnetoresistance in LaBi: Origin of field-induced resistivity upturn and plateau in compensated semimetals, New J. Phys. **18**, 082002 (2016).

[48] S. Chatterjee, S. Khalid, H. S. Inbar, A. Goswami, F. C. de Lima, A. Sharan, F. P. Sabino, T. L. Brown-Heft, Y.-H. Chang, A. V. Fedorov, D. Read, A. Janotti, and C. J. Palmstrøm, Weak anti-localization in quasi-two-dimensional electronic states of epitaxial LuSb thin films, Phys. Rev. B **99**, 125134 (2019).

[49] S. Hikami, A. I. Larkin, and Y. Nagaoka, Spin-orbit interaction and magnetoresistance in the two dimensional random system, Prog. Theor. Phys. **63**, 707 (1980).

[50] P. W. Anderson, Absence of diffusion in certain random lattices, Phys. Rev. **109**, 1492 (1958).

[51] K. Nomura and N. Nagaosa, Surface-Quantized Anomalous Hall Current and the Magnetoelectric Effect in Magnetically Disordered Topological Insulators, Phys. Rev. Lett. **106**, 166802 (2011).

[52] S. Xiao, D. Wei, and X. Jin, Bi(111) Thin Film with Insulating Interior but Metallic Surfaces, Phys. Rev. Lett. **109**, 166805 (2012).

[53] F. Wang and Y. Ran, Nearly flat band with Chern number $C = 2$ on the dice lattice, Phy. Rev. B **84**, 241103(R) (2011).

[54] T. H. Hsieh, H. Lin, J. Liu, W. Duan, A. Bansil, and L. Fu, Topological crystalline insulators in the SnTe material class, Nat. Commun. **3**, 982 (2012).

[55] J. Liu, Y. Xu, J. Wu, B.-L. Gu, S. B. Zhang, and W. Duan, Manipulating topological phase transition by strain, Acta Cryst. C **70**, 118 (2014).

[56] R. Yu, W. Zhang, H.-J. Zhang, S.-C. Zhang, X. Dai, and Z. Fang, Quantized anomalous Hall effect in magnetic topological insulators, Science **329**, 61 (2010).

[57] F. D. M. Haldane, Model for a Quantum Hall Effect without Landau Levels: Condensed-Matter Realization of the "Parity Anomaly", Phys. Rev. Lett. **61**, 2015 (1988).

[58] J. G. Checkelsky, R. Yoshimi, A. Tsukazaki, K. S. Takahashi, Y. Kozuka, J. Falson, M. Kawasaki, and Y. Tokura, Trajectory of the anomalous Hall effect towards the quantized state in a ferromagnetic topological insulator, Nat. Phys. **10**, 731 (2014).

[59] J. L. Collins, A. Tadich, W. Wu, L. C. Gomes, J. N. B. Rodrigues, C. Liu, J. Hellerstedt, H. Ryu, S. Tang, S. K. Mo, S. Adam, S. A. Yang, M. S. Fuhrer, and M. T. Edmonds, Electric-field-tuned topological phase transition in ultrathin Na_3Bi, Nature **564**, 390 (2018).

[60] J. Rossat-Mignod, P. Burlet, S. Quezel, J. M. Effantin, D. Delacôte, H. Bartholin, O. Vogt, and D. Ravot, Magnetic properties of cerium monopnictides, J. Magn. Magn. Mater. **31–34**, 398 (1983).

[61] F. Hulliger, H. R. Ott, and T. Siegrist, Low temperature behavior of HoBi, J. Less Common Met. **96**, 263 (1984).

[62] A. Fente, H. Suderow, S. Vieira, N. M. Nemes, M. García-Hernández, S. L. Bud'ko, and P. C. Canfield, Low temperature magnetic transitions of single crystal HoBi, Solid State Commun. **171**, 59 (2013).